7. A. I. Kingon, J.-P Maria, S. K. Streiffer, *Nature* **406**, 1032 (2000).

8. S. M. George *et al.*, *Appl. Surf. Sci.* **82–83**, 460 (1994).

9. W. Gasser, Y. Uchida, M. Matsumura, *Thin Solid Films* **250**, 213 (1994).

10. S. Morishita, W. Gasser, K. Usami, M. Matsumura, *J. Non-Cryst. Solids* **187**, 66 (1995).

11. K. Yamaguchi *et al.*, *Appl. Surf. Sci.* **130–132**, 202 (1998).

12. J. W. Klaus, O. Sneh, A. W. Ott, S. M. George, *Surf. Rev. Lett.* **6**, 435 (1999).

13. J. D. Ferguson, A. W. Weimer, S. M. George, *Appl. Surf. Sci.* **162–163**, 280 (2000).

14. _____, *Chem. Mater.* **12**, 3472 (2000).

15. J. W. Klaus, S. M. George, *Surf. Sci.* **447**, 81 (2000).

16. M. Ylilammi, *Thin Solid Films* **279**, 124 (1996).

17. J.-W. Lim, J.-S. Park, S.-W. Kang, *J. Appl. Phys.* **87**, 4632 (2000).

18. J.-S. Min *et al.*, *Jpn. J. Appl. Phys., Part 1* **37**, 4999 (1998).

19. Me$_3$Al from Albemarle Corporation (Baton Rouge, LA) was held at 25°C, at which temperature its vapor pressure is ∼15 torr.

20. This was prepared by the method described in (*43*) and also obtained from Aldrich Chemical Company (Milwaukee, WI) and Gelest Inc. (Morrisville, PA) and heated to 115°C, at which temperature it has a vapor pressure of ∼20 torr.

21. To deliver pulses of Me$_3$Al vapor, we opened a three-way valve, with inner channels of 0.4-mm inner diameter, to Me$_3$Al vapor for 1 s, during which time 1 μmol of Me$_3$Al vapor flowed into the deposition chamber. Then, the three-way valve was turned to flow nitrogen for 5 s to purge the chamber of residual unreacted Me$_3$Al vapor. To deliver (Bu^{t}O)$_3$SiOH vapor, we filled a 35-ml volume with (Bu^{t}O)$_3$SiOH vapor at its equilibrium vapor pressure (ranging from 3.1 to 100 torr at reservoir temperatures from 80° to 150°C). A valve between the deposition chamber and the vacuum pump was closed, and a valve between the 35-ml volume and the deposition chamber was opened to allow the measured dose of (Bu^{t}O)$_3$SiOH vapor to expand into the deposition chamber. After 15 s, the valve to the pump was opened, and nitrogen was flowed for 5 s to purge the chamber of excess (Bu^{t}O)$_3$SiOH, as well as of volatile by-products of the reaction. This cycle was then repeated. At the end of the prescribed number of cycles (typically 4 to 100), substrates of silicon, glass, and glassy carbon were removed from the reactor. Identical results were found for other experiments in which the 15-s exposure time to (Bu^{t}O)$_3$SiOH was increased to 90 s.

22. Silicon substrates were prepared by removing the native oxide with dilute hydrofluoric acid solution. Then the substrates were irradiated with ultraviolet light (from a mercury lamp) in air until the surface became hydrophilic (normally a couple of minutes).

23. Roughness measurements by atomic force microscopy [Digital Instruments (Santa Barbara, CA) and ThermoMicroscopes (Sunnyvale, CA)] showed that the films are just as smooth as their substrates.

24. Composition and number of atoms per unit area were determined by Rutherford backscattering spectroscopy [General Ionics Model 4117, 1.7 MeV Tandetron (Coyahoga Falls, OH)] of samples grown on glassy carbon substrates.

25. Thickness and refractive index were determined by ellipsometry [Rudolf Auto-El II (Flanders, NJ)]. Thickness and density were also found by low-angle x-ray reflection [Scintag Model XDS2000 (Cupertino, CA)].

26. In Fig. 1, the film thicknesses plotted for the underdosed experiments are the average over the whole length (30 cm) of the reactor tube. The film thickness near the entry point for the vapors still has the saturated value even for the underdosed conditions.

27. The microbalance used was an Inficon Technologies (East Syracuse, NY) bakeable quartz crystal microbalance.

28. The coating is uniform within the measurement accuracy of about ±3 nm for SEMs on a cleaved cross section.

29. X-ray scattering (Scintag Model XDS2000) and electron diffraction by transmission electron microscopy [JEOL 2010F (Peabody, MA)] determined that the films are amorphous.

30. Measured on capacitors formed by e-beam evaporation of platinum dots through a shadow mask.

31. This estimate of a monolayer thickness was obtained by taking the cube root of the volume occupied by a formula unit of SiO$_2$ in material with density of 2.0 g/cm^3.

32. A. C. Dillon, A. W. Ott, J. D. Way, S. M. George, *Surf. Sci.* **322**, 230 (1995).

33. M. Juppo, A. Rahtu, M. Ritala, M. Leskela, *Langmuir* **16**, 4034 (2000).

34. A. Rahtu, T. Alaranta, M. Ritala, *Langmuir* **17**, 6506 (2001).

35. A reaction that may be somewhat analogous to this step is the polymerization of a different silanol in solution as reported in (*44*).

36. K. W. Terry, P. K. Ganzel, T. D. Tilley, *Chem. Mater.* **4**, 1290 (1992).

37. C. G. Lugmair, K. L. Fujdala, T. D. Tilley, *Chem. Mater.* **14**, 888 (2002).

38. M. G. Voronkov, A. N. Lazarev, A. K. Baigozhin, *Zh. Obshch. Khim.* **26**, 3072 (1956) (Engl. transl., p. 3421).

39. G. Schott, L. Engelbrecht, H. J. Holdt, *Z. Anorg. Allg. Chem.* **459**, 177 (1979).

40. M. J. Frisch *et al.*, Gaussian 98 (Revision A.9) (Gaussian Inc., Pittsburgh, PA, 1998).

41. The system was simplified by using hydrogen atoms to terminate bonds that were more than two bonds away from the reaction center. The aluminum catalytic center was modeled as Al(OH)$_3$. On the (Bu^{t}O)$_3$SiOH, the two butoxy groups not involved in the initial chemisorption reaction are replaced by hydroxyl groups. The butoxy group that is initially cleaved as *tert*-butanol was simplified to a methyl group leaving as methanol. The structures and energies of the reactants, products, and transition state were calculated by the Gaussian program with density functional theory B3LYP using a very large basis set, 6-311++G(3df,3pd)//6-31+G(d).

42. R. G. Gordon, J. Becker, D. Hausmann, S. Suh, *Chem. Mater.* **13**, 2463 (2001).

43. Y. Abe, I. Kijima, *Bull. Chem. Soc. Jpn.* **42**, 1118 (1969).

44. J. H. Gaul, T. M. Carr, *Spec. Lett.* **16**, 651 (1983).

45. The etched wafer and the SEMs of the coated holes shown in Fig. 3 were supplied by M. Gutsche of Infineon Technologies (Munich, Germany). The SEM of the uncoated hole was taken by P. de Rouffignac. This work was supported in part by the NSF.

2 May 2002; accepted 9 September 2002

Role of ANC-1 in Tethering Nuclei to the Actin Cytoskeleton

Daniel A. Starr and Min Han*

Mutations in *anc-1* (nuclear anchorage defective) disrupt the positioning of nuclei and mitochondria in *Caenorhabditis elegans*. ANC-1 is shown to consist of mostly coiled regions with a nuclear envelope localization domain (called the KASH domain) and an actin-binding domain; this structure was conserved with the *Drosophila* protein Msp-300 and the mammalian Syne proteins. Antibodies against ANC-1 localized cytoplasmically and were enriched at the nuclear periphery in an UNC-84–dependent manner. Overexpression of the KASH domain or the actin-binding domain caused a dominant negative anchorage defect. Thus, ANC-1 may connect nuclei to the cytoskeleton by interacting with UNC-84 at the nuclear envelope and with actin in the cytoplasm.

A wide variety of organisms have syncytia, formed either when multiple nuclear divisions occur without cell divisions or when cells fuse together. Normally, syncytial nuclei are located in specific regions or are evenly spaced throughout the cytoplasm. Nuclear positioning is also essential to a variety of singly nucleated polar cells and even in single-celled organisms (*1*). Microtubules and associated dynein and kinesin motors play a central role in the positioning of nuclei (*2*). Less is known about the role of actin in the process of nuclear positioning. However, a defect in the actin cytoskeleton of nurse cells of *Drosophila* oocytes disrupts nuclear anchorage during cytoplasmic dumping (*3*). Actin is also required for plant nuclear migrations (*4*). We used the large syncytial cells of *C. elegans* as a model to study the mechanism of nuclear anchorage. Most of the body

of an adult worm is covered by four large syncytial hypodermal cells that contain more than 100 nuclei (*5*). Normally, nuclei are evenly spaced throughout the syncytia. However, mutations in either *anc-1* or *unc-84* cause an Anc phenotype, in which nuclei float freely within the cytoplasm of syncytial cells and often group together (*6*, *7*). The Anc phenotype is observed in all somatic, postembryonic syncytial cells, even in binucleated intestinal cells (*7*).

We determined the molecular identity of *anc-1* (*8*). RNA interference (RNAi) experiments and the identification of a molecular lesion in the predicted open reading frame of *anc-1(e1873)* confirmed that we had cloned *anc-1* (*8*) (Fig. 1, A to D, and fig. S1). The full-length cDNA of *anc-1* was predicted to be 25,639 base pairs (bp) encoding an 8546-residue protein. The bulk of ANC-1 (the *anc-1* gene product) consisted of mostly predicted coiled regions, including six repeats of 903 residues that are essentially identical at the nucleotide level (supporting online text). The length of the repeat region may be maintained because of a selective advantage of keeping ANC-1 large.

Howard Hughes Medical Institute and Department of Molecular, Cellular and Developmental Biology, University of Colorado, Boulder, CO 80309, USA.

*To whom correspondence should be addressed. E-mail: mhan@colorado.edu

Fig. 1. Nomarski photographs of the lateral syncytial hypodermis of L2 hermaphrodites. Selected nuclei are marked with arrows. (**A**) *N2* animal. (**B**) *anc-1(e1873)* animal. (**C**) RNAi-treated animal from a mother injected with double-stranded RNA (dsRNA) against exons 13 to 18 of *anc-1*. dsRNA against a full repeat of *anc-1* or the five exons at the 3′ end of *anc-1* gave similar results. Scale bar, 10 μm. (**D**) The predicted intron/exon structure of *anc-1*. The site of the *anc-1(e1873)* molecular lesion is marked by an arrow. Sequenced cDNAs that were identified either by expressed sequence tags or as RT-PCR products (*8*) are depicted below the structure (**E**) A depiction of the predicted domains of ANC-1 and related proteins. All shades of blue represent regions highly predicted to be helical, with interspersed regions of predicted coiled-coil domains. The dark blue regions of the Syne proteins and of Msp-300 represent spectrin repeats. The mid-shade blue in ANC-1 represents repetitive regions. The conserved KASH domain at the COOH-terminus is yellow. Black arrowheads mark predicted transmembrane domains. The NH$_2$-terminal regions with homology to calponin-type actin-binding domains are red. Some of the Syne protein sequences were deduced from genome projects (supporting online text). Human Syne-2 corresponds to NUANCE (*14*).
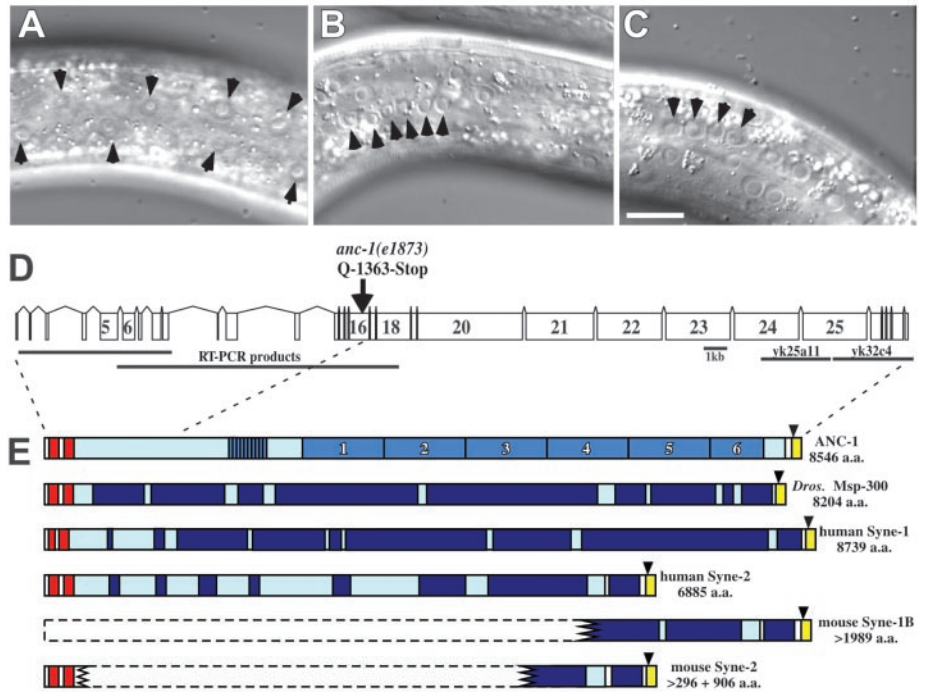
This could allow a single ANC-1 molecule to extend more than 0.5 μm, long enough to stretch between the nucleus and the actin cytoskeleton. The COOH-terminal 60 residues of ANC-1 were found to be conserved with the COOH-termini of *Drosophila* Klarsicht (*9, 10*) and of mammalian Syne-1 and Syne-2 (supporting online text, Fig. 1E, and fig. S2) (*11–14*). We call this the KASH domain (for Klarsicht/ANC-1/Syne-1 homology). We showed by reverse transcription–polymerase chain reaction (RT-PCR) that the *Drosophila* CK00024 sequence, located nearly 45 kbp downstream of the previously known 3′ end of the *msp-300* transcript (*15, 16*), is part of the *msp-300* gene. Syne-1 and Syne-2 (synaptic nuclei expressed, also known as Myne, Nesprin, and NUANCE) localize to the nuclear envelope of mouse and human muscle cells throughout development (*11–14*). The KASH domains of Syne-1 and Syne-2 are sufficient for nuclear envelope targeting in tissue culture cells (*13, 14*). Syne-1 is enriched at the nuclear envelope of myonuclei clustered at the neuromuscular junction, which suggests a role in nuclear positioning at the synapse (*11*). Msp-300, Syne-1, and Syne-2 have large central domains of multiple spectrin repeats that could function analogously to the long coiled domains of ANC-1 (*17*). The NH$_2$-terminus of ANC-1 is also similar to that of Msp-300 and the Syne proteins, containing two approximately 100–amino-acid stretches of homology to the calponin domains of human alpha-actinin (supporting online text, Fig. 1E, and fig. S2). Calponin domains are actin-binding motifs (*18*), suggesting that the NH$_2$-terminal domain of ANC-1 interacts with the actin cytoskeleton.

Fig. 2. (**A**) Affinity-purified antibodies to ANC-1 were used to probe an immunoblot from a 5% acrylamide gel. Antibodies recognized multiple bands that migrate more slowly than the 175-kD marker. (**B** and **C**) ANC-1 antibody localization is pseudocolored red and 4′,6′-diamidino-2-phenylindole (DAPI)–stained nuclei are blue. (B) The lateral surface of the mid-body of an L4 *N2* worm. ANC-1 antibodies localized to the cytoplasm and were enriched at the nuclear periphery. (C) The extruded gut of an *N2* adult. (**D**) The molecular lesions in UNC-84 that were tested for their ability to disrupt ANC-1 localization. The conserved SUN domain of UNC-84 is shaded. (**E** and **F**) Samples shown are of extruded uterine tissue from (**E**) *unc-84(n399)* or (**F**) *unc-84(e1411)* adult hermaphrodites. Arrows point to examples of uterine nuclei. Scale bars, 10 μm. ANC-1 localization was tested in 11 mutant strains (supporting online text).
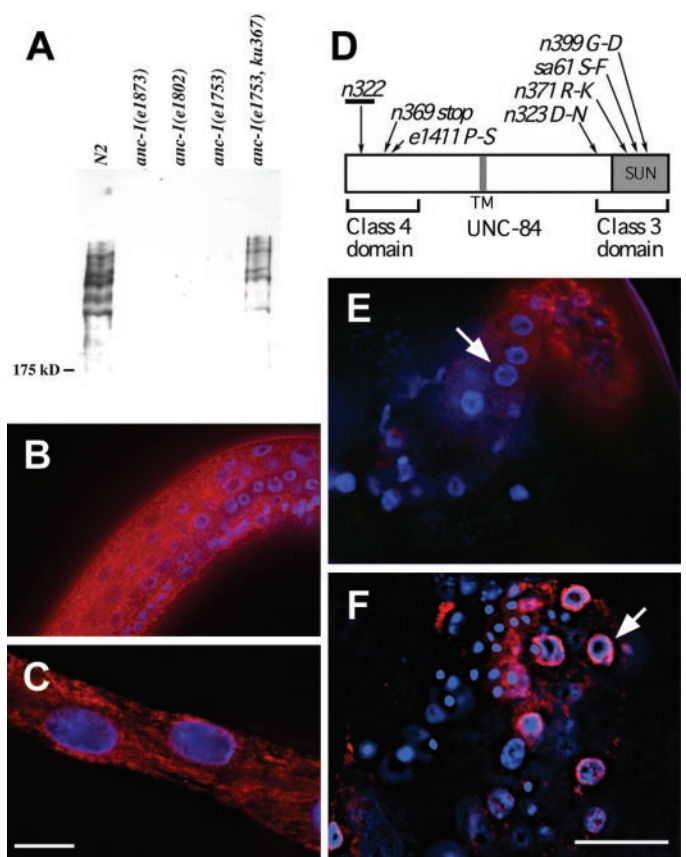
Antibodies were raised against the tandem repeat region of ANC-1; the specificity of the affinity-purified antibody was shown by immunoblot analysis (Fig. 2A) and by the fact that purified antibodies in *anc-1* mutant tissues failed to localize. ANC-1 was first detected in

L1 larvae and was observed through adult stages where antibodies localized to the cytoplasm of all postembryonic somatic cells (Fig. 2, B and C). Peripheral nuclear localization of ANC-1 was observed in a variety of cells, including uterine cells. The nuclear envelope component UNC-84 is required for nuclear migration and anchorage (6, 19, 20). We tested whether ANC-1 localized properly in a collection of unc-84 mutant backgrounds. ANC-1 failed to localize to the nuclear periphery in the null unc-84 allele and in alleles that have missense mutations in or near the conserved SUN (for Sad1p, UNC-84 homology) domain of UNC-84 and that disrupt both nuclear migration and anchorage (6) (Fig. 2E). In contrast, ANC-1 was detected at the nuclear envelope in unc-84 alleles that have missense mutations or small deletions in the NH$_2$-terminus of UNC-84 and that disrupt only migration (6) (Fig. 2F). ANC-1 was still detected at normal levels in the cytoplasm in all unc-84 mutants. Thus the UNC-84 SUN domain is required for ANC-1 localization to the nuclear envelope but not for overall ANC-1 levels. UNC-83, a component required for nuclear migration, also localizes to the nuclear envelope in an UNC-84–dependent manner (21). The predicted transmembrane domains in both ANC-1 and UNC-83 may play important roles in localization or maintenance of the proteins at the nuclear envelope, as appears to be the case for Syne-1 (13).

There may be a limited number of ANC-1 docking sites at the nuclear envelope. To test this possibility, we bred animals that overexpressed the COOH-terminal 346 residues of ANC-1, including the KASH domain, using a heat shock promoter. Heat shock of these transgenic animals for 2 hours caused a strong nuclear anchorage defect in 100% of larval animals (Fig. 3C). In addition, staining with hemagglutinin (HA) epitope antibodies showed that the COOH-terminal domain of ANC-1 localized to the nuclear envelope (Fig. 3, H to J). As a control, overexpression of an 1887–amino acid fragment in the middle of ANC-1 did not cause any detectable mutant phenotype (Fig. 3B). Thus, multiple ANC-1 molecules are required to bind to a limited number of docking sites at the nuclear envelope, suggesting that the overexpressed domain blocks endogenous ANC-1 from docking at the nuclear envelope. This is likely to occur by disrupting the interaction between UNC-84 and ANC-1. However, we were unable to detect a direct physical interaction between the SUN domain of UNC-84 and the COOH-terminal domain of ANC-1 using the two-hybrid system or by glutathione S-transferase pull-down assays. Thus, UNC-84 may function through other proteins to recruit or maintain ANC-1 at the nuclear envelope.

To determine whether ANC-1 could bind directly to actin, an in vitro F-actin binding assay was performed. The NH$_2$-terminal domain of ANC-1 was shown to bind to fila-
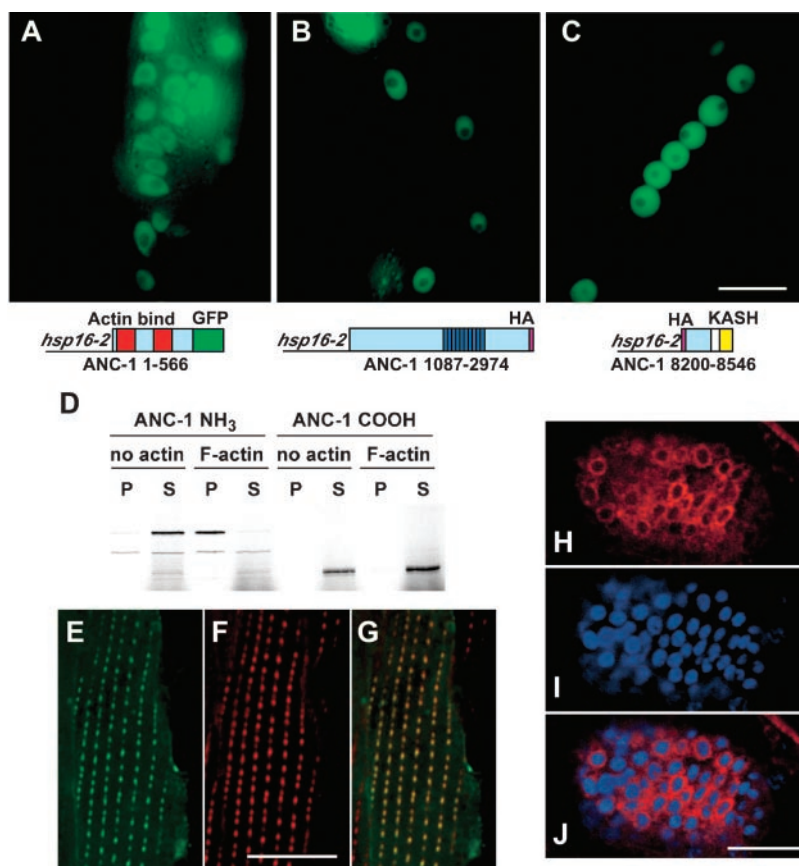

Fig. 3. (**A** to **C**) Hypodermal nuclei (green) of L4 animals were identified by the coinjection marker protein SUR-5::GFP. Schematic figures of the constructs are shown at the bottom of the panels. Overexpression of (A) the NH$_2$-terminus or (C) the COOH-terminus, but not (B) a middle region, of ANC-1 caused a nuclear anchorage defect. (**D**) An autoradiograph is shown detecting [^{35}S]methionine-labeled end domains of ANC-1. Lanes with equally loaded pellets (P) and supernatants (S) are coupled. The presence of actin filaments (F actin) is noted above. The left-hand lanes show that the NH$_2$-terminal 700 residues of ANC-1 bound to filamentous actin. The right-hand lanes show that the COOH-terminal 346 residues of ANC-1 did not bind to actin filaments. (**E** to **G**) An adult body wall muscle is shown in a worm expressing the NH$_2$-terminal 566 residues of ANC-1 fused to GFP, expressed from a heat shock promoter after 2 hours at 33°C. (**E**) GFP fluorescence and (**F**) actin filaments stained with phalloidin colored red. (**G**) Colocalization is shown in yellow. (**H** to **J**) An embryo overexpressing the COOH-terminal domain of ANC-1 stained with (**H**) antibodies against the HA epitope, pseudocolored red, or (**I**) DAPI, colored blue, to show nuclei. (**J**) The merged image. Scale bars, 10 μm.

mentous actin but not to monomeric actin (Fig. 3D). The NH$_2$-domains of MSP-300 and Syne-2 also bind actin in vitro (14, 15). The conserved nature of the NH$_2$-terminus of ANC-1 suggests that ANC-1 binds actin in vivo. To test this, the NH$_2$-terminal 566 residues of ANC-1 were fused to green fluorescent protein (GFP) and expressed in worms from a heat shock promoter. When subjected to a short heat shock at 33°C for 2 hours, the NH$_2$-terminal ANC-1::GFP completely colocalized with actin in body wall muscles (Fig. 3, E to G), suggesting that the in vitro actin-binding activity is functional in the cell. The analogous construct of human Syne-2 also binds actin in vitro and colocalizes with actin in tissue culture (14). Long-term overexpression of NH$_2$-terminal ANC-1::GFP led to a paralyzed and arrested elongation at twofold (Pat) phenotype, in which embryos failed to elongate because of blocked muscle develop-

ment (supporting online text and fig. S3). Overexpression of the NH$_2$-terminus of ANC-1 by a stronger heat shock caused a weak Anc phenotype; clumps of at least three hypodermal nuclei were observed in 23% of larval animals (n = 77), whereas 4% of worms had a severe Anc phenotype (Fig. 3A). The lack of a more severe dominant Anc phenotype in the syncytial hypodermis may be due to the lower expression level of the transgene in hypodermal cell lineages, as judged by GFP expression, or due to an abundance of actin-binding sites available for ANC-1 in these cells.

Mutations in anc-1 disrupt the positioning and shape of mitochondria (7). We examined this phenotype in live animals using a GFP construct targeted to the mitochondria of body wall muscles (22). In wild-type animals, mitochondria appeared long and string-like (Fig. 4A). The mitochondria also remained anchored
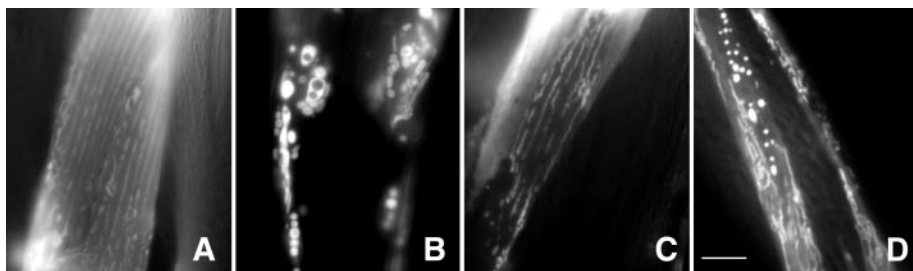
Fig. 4. GFP-labeled mitochondria are shown in the body wall muscle cells of L4 animals of the following genotypes: (**A**) wild-type *N2*, (**B**) *anc-1(e1873)*, (**C**) *unc-84(n369)*, and (**D**) cofilin *unc-60(r398)*. The severely abnormal mitochondria in *anc-1(e1873)* are not anchored. In live animals, they were seen moving throughout the muscle as the animal moved. Scale bar, 10 μm.

and spread throughout the cell as the worm moved. In contrast, mitochondria in *anc-1(e1873)* animals were spherically shaped, often clustered together, and were pushed around within the cytoplasm as the animal moved (Fig. 4B). Mitochondria were not shaped or positioned properly in an *unc-60(r398)* mutant background (Fig. 4D). A partial loss-of-function allele in the *C. elegans* cofilin homolog, *unc-60(r398)*, disrupts actin filaments in the body wall muscle of adult hermaphrodites (*23*). Therefore, actin filaments are required for proper positioning of mitochondria. The anchorage of mitochondria in *unc-84(n369)* was normal (Fig. 4C), suggesting that ANC-1 does not require UNC-84 to anchor mitochondria as it does for nuclear anchorage.

Our model (fig. S4) suggests that ANC-1 functions to anchor nuclei by tethering the nucleus to the actin cytoskeleton and predicts that the KASH domain of ANC-1 is localized to the outer nuclear envelope by UNC-84. Digitonin extraction experiments show that human Syne-2 localizes to the outer nuclear envelope (*14*). ANC-1 would then extend away from the nucleus, where its NH_2-terminus binds to the stable actin cytoskeleton. As a result, ANC-1 molecules function to directly attach the actin cytoskeleton to the nuclear envelope. Before a nucleus can migrate through the cytoplasm of the cell, the nuclear anchor must be released. The SUN domain of UNC-84 is likely to be intimately involved with this switch in nuclear behavior, because it is required for both ANC-1 and UNC-83 localization at the nuclear envelope (*21*) (Fig. 2). UNC-83 is required for normal nuclear migration but not for nuclear anchorage (*21*). It is not known whether ANC-1 and UNC-83 can interact with UNC-84 simultaneously, although both antigens are detected at the nuclear envelope of adult hypodermal cells. Overexpression of UNC-83 did not cause any obvious anchorage phenotype, eliminating a competition model.

Dystrophin and the associated dystrophin–glycoprotein complex function to connect the actin cytoskeleton to the extracellular matrix; mutations in these components lead to Duchenne or Becker muscular dystrophies (*24*). Although ANC-1 and Syne connect the actin cytoskeleton to the nuclear matrix whereas dystrophin connects actin to the extracellular matrix, there are some similarities between these two mechanisms. ANC-1 and associated proteins, including UNC-84 and lamin A/C (*12*), are likely to create a bridge across the nuclear envelope. Mutations in the gene encoding lamin A/C lead to Emery-Dreifuss muscular dystrophy (*24*), which suggests a potential link between the ANC-1 and Syne proteins and muscular dystrophy.

References and Notes

1. N. R. Morris, *J. Cell Biol.* **148**, 1097 (2000).
2. S. Reinsch, P. Gonczy, *J. Cell Sci.* **111**, 2283 (1998).
3. G. M. Guild, P. S. Connelly, M. K. Shaw, L. G. Tilney, *J. Cell Biol.* **138**, 783 (1997).
4. E. Chytilova *et al.*, *Mol. Biol. Cell* **11**, 2733 (2000).
5. J. E. Sulston, H. R. Horvitz, *Dev. Biol.* **56**, 110 (1977).
6. C. J. Malone, W. D. Fixsen, H. R. Horvitz, M. Han, *Development* **126**, 3171 (1999).
7. E. M. Hedgecock, J. N. Thomson, *Cell* **30**, 321 (1982).
8. Materials and methods are available as supporting material on *Science* Online.
9. K. L. Mosley-Bishop, Q. Li, L. Patterson, J. A. Fischer, *Curr. Biol.* **9**, 1211 (1999).
10. M. A. Welte, S. P. Gross, M. Postner, S. M. Block, E. F. Wieschaus, *Cell* **92**, 547 (1998).
11. E. D. Apel, R. M. Lewis, R. M. Grady, J. R. Sanes, *J. Biol. Chem.* **275**, 31986 (2000).
12. J. M. Mislow, M. S. Kim, D. B. Davis, E. M. McNally, *J. Cell Sci.* **115**, 61 (2002).
13. Q. Zhang *et al.*, *J. Cell Sci.* **114**, 4485 (2001).
14. Y. Y. Zhen, T. Libotte, M. Munck, A. A. Noegel, E. Korenbaum, *J. Cell Sci.* **115**, 3207 (2002).
15. Y. Rosenberg-Hasson, M. Renert-Pasca, T. Volk, *Mech. Dev.* **60**, 83 (1996).
16. T. Volk, *Development* **116**, 721 (1992).
17. Y. Yan *et al.*, *Science* **262**, 2027 (1993).
18. M. Gimona, K. Djinovic-Carugo, W. J. Kranewitter, S. J. Winder, *FEBS Lett.* **513**, 98 (2002).
19. H. R. Horvitz, J. E. Sulston, *Genetics* **96**, 435 (1980).
20. K. K. Lee *et al.*, *Mol. Biol. Cell* **13**, 892 (2002).
21. D. A. Starr *et al.*, *Development* **128**, 5039 (2001).
22. A. Fire *et al.*, *Nature* **391**, 806 (1998).
23. S. Ono, D. L. Baillie, G. M. Benian, *J. Cell Biol.* **145**, 491 (1999).
24. E. A. Burton, K. E. Davies, *Cell* **108**, 5 (2002).
25. We thank Han lab members and L. Chen for their advice; S. McCauley, G. Ackerman, and L. Chlipala for technical assistance; and the *Caenorhabditis* Genetics Center, J. Hodgkin, S. Ono, P. Mains, A. Fire, A. Coulson, and Y. Kohara for materials. Supported by NIH and Howard Hughes Medical Institute.

Neural Correlates for Perception of 3D Surface Orientation from Texture Gradient

Ken-Ichiro Tsutsui,[1]* **Hideo Sakata,**[1,2] **Tomoka Naganuma,**[1,3] **Masato Taira**[1]†

A goal in visual neuroscience is to reveal how the visual system reconstructs the three-dimensional (3D) representation of the world from two-dimensional retinal images. Although the importance of texture gradient cues in the process of 3D vision has been pointed out, most studies concentrate on the neural process based on binocular disparity. We report the neural correlates of depth perception from texture gradient in the cortex. In the caudal part of the lateral bank of intraparietal sulcus, many neurons were selective to 3D surface orientation defined by texture gradient, and their response was invariant over different types of texture pattern. Most of these neurons were also sensitive to a disparity gradient, suggesting that they integrate texture and disparity gradient signals to construct a generalized representation of 3D surface orientation.

The real world is three-dimensional (3D), but when projected to the retina it is reduced to a two-dimensional (2D) image. Nevertheless, what we see and what we perceive is all 3D. Therefore, the brain must be reconstructing the 3D representation of the real world from the 2D images on the retinae. Among many kinds of depth cues, binocular disparity has been suggested to be critical in many psychophysical studies (*1–3*). Neurons in striate (*4–7*) and extrastriate (*6–10*) visual areas are sensitive to binocular disparity signals. Recently, neurons that code 3D features of a visual surface by higher-order processing of